$Ni_2Mo_3O_8$: Complex antiferromagnetic order on a honeycomb lattice

Jennifer R. Morey,[1,2] Allen Scheie,[2] John P. Sheckelton,[1,2] Craig M. Brown,[3] and Tyrel M. McQueen[1,2,4]
[1]*Department of Chemistry, Johns Hopkins University, Baltimore, Maryland 21218, USA*
[2]*Institute for Quantum Matter, Department of Physics and Astronomy, Johns Hopkins University, Baltimore, Maryland 21218, USA*
[3]*National Institute for Standards and Technology, Gaithersburg, Maryland 20899, USA*
and Department of Chemical and Biomolecular Engineering, University of Delaware, Newark, Delaware 19716, USA
[4]*Department of Materials Science and Engineering, Johns Hopkins University, Baltimore, Maryland 21218, USA*

(Received 12 April 2018; revised manuscript received 10 September 2018; published 18 January 2019)

Theoretical studies have predicted the existence of topological magnons in honeycomb compounds with stripy or zigzag antiferromagnetic (AFM) order. Here we report the discovery of AFM order in the layered and noncentrosymmetric honeycomb nickelate $Ni_2Mo_3O_8$ through a combination of magnetization, specific heat, x-ray and neutron diffraction, and electron paramagnetic resonance measurements. The AFM order is complex, with a mixture of stripy and zigzag character on an integer spin noncentrosymmetric honeycomb lattice ($P6_3mc$). Further, each of the two sublattices of the bipartite honeycomb lattice is comprised of a different crystal field environment, i.e., octahedral and tetrahedral Ni^{2+}, respectively, enabling independent substitution on each. Replacement of Ni by Mg on the octahedral site suppresses the long-range magnetic order and results in a weakly ferromagnetic state. Conversely, substitution of Fe for Ni enhances the strength of the AFM exchange and increases the ordering temperature. Thus, $Ni_2Mo_3O_8$ provides a platform on which to explore the rich physics of $S = 1$ on the honeycomb lattice in the presence of competing magnetic interactions with a noncentrosymmetric, formally piezopolar, crystal structure.

DOI: 10.1103/PhysRevMaterials.3.014410

I. INTRODUCTION

The prediction and discovery of topological phenomena in materials have ignited a global search for new quantum materials and states of matter [1,2], with potential applications in quantum computing and information storage. The physical realization of theoretically proposed topological states requires the ability to produce materials with highly controlled structural, electronic, and magnetic properties. Most materials release inherent magnetic degeneracy at sufficiently low temperatures by mechanisms such as structural phase transitions, local magnetic ordering, and changes in the degree of electron localization (e.g., by the formation of singlet pairs with neighboring ions), but there are some states of matter postulated to retain finite degeneracy to $T = 0\,\mathrm{K}$, such as quantum spin liquids (QSLs) [3–6].

One of the main structure types known to host quantum frustrated magnetic topological phenomena is the "honeycomb" structure, which is a two-dimensional bipartite lattice. Unlike the triangular lattice or spinel structure, the honeycomb is not inherently geometrically frustrated but becomes frustrated in the presence of competing longer-range magnetic interactions or anisotropic magnetic exchanges. One example of this is the ruthenium honeycomb in α-$RuCl_3$ which may host almost exactly the interactions that allow a Kitaev QSL state to emerge [7–11]. It is suggested that it is strong next-nearest-neighbor and next-next-nearest-neighbor interactions that stabilize frustration in this material [12,13]. Furthermore, extensive experimental and theoretical investigations into iridium honeycomb compounds Li_2IrO_3 [14–18] and Na_2IrO_3 [19–23] have realized many of the types of magnetically ordered states that are proximal to QSL states—i.e., stripy and zigzag antiferromagnetism (AFM) [17,24–28].

The nature of the spin interaction, relevant magnetic exchanges, structural geometry, order, symmetry, and spin-orbit coupling (SOC) influence the magnetic ground state of a compound. SOC generally increases with atomic number and becomes a controlling factor in 4*d* and 5*d* transition-metal honeycombs, particularly those incorporating iridium and ruthenium. It has been posited that the ground state in the iridium honeycombs is not a QSL, but rather is magnetically ordered due to strong SOC [28].

Despite having weaker SOC than the 4*d* or 5*d* equivalents, 3*d* ions with strong anisotropy, e.g., Co^{2+}, may also harbor strong bond-dependent interactions between ions [29,30]. Further, recent theoretical predictions have shown that honeycomb compounds with zigzag AFM and stripy AFM order may host topologically nontrivial magnons that are robust against next-nearest-neighbor Dzyaloshinskii-Moriya (DM) interactions [31,32]. Less clear theoretically is the impact of nearest-neighbor DM interactions (which are also permitted in a noncentrosymmetric structure) on the topological magnons, with some work suggesting an inversion of the topological nature when it is sufficiently strong [33], offering the opportunity to tune through a topological transition by modulating the strength of the nearest-neighbor DM interaction (by controlling the degree of noncentrosymmetry).

Here we report that $Ni_2Mo_3O_8$, which contains a honeycomb of $S = 1$ Ni^{2+} ions and has previously been reported to remain paramagnetic down to $T = 2\,\mathrm{K}$ [34], undergoes a transition to a magnetically ordered antiferromagnetic state below $T_N = 6\,\mathrm{K}$. Compared to other nickel compounds known to

have zigzag antiferromagnetic order, including $BaNi_2V_2O_8$, $BaNi_2As_2O_8$, $Na_3Ni_2BiO_6$, $A_3Ni_2SbO_6$ (A = Li, Na), and $Cu_3Ni_2SbO_6$ [35–37], $Ni_2Mo_3O_8$ is different: (a) the two triangular sublattices of the honeycomb have different local coordination environments of the Ni^{2+} ions (octahedral and tetrahedral), permitting selective replacement of one of the two halves of the bipartite lattice, and (b) the order is an admixture of stripy and zigzag order. Additionally, it is an example of non-Néel AFM order in a noncentrosymmetric $S = 1$ honeycomb material, complementing the only other known noncentrosymmetric zigzag AFM material, $Na_2Co_2TeO_6$, with $S = 3/2$.

In $Ni_2Mo_3O_8$, we find that substitution of nonmagnetic Mg^{2+} on the tetrahedral site removes long-range magnetic order, with remnant small ferromagnetic interactions between Ni^{2+} ions. In contrast, substitution of $S = 2$ Fe^{2+} for Ni^{2+} results in a large increase in the antiferromagnetic ordering temperature to $T_N = 50$ K. The ability to selectively substitute one of the two sites in the honeycomb makes this material an excellent platform from which to investigate the underlying physics of the selection of magnetic ground states on the $S = 1$ honeycomb lattice, similar to what has recently been demonstrated for $S = 2$ $Fe_2Mo_3O_8$ [38].

II. EXPERIMENTAL METHODS

A. Powder synthesis

$M_2Mo_3O_8$, M = (Mg, Ni, Fe, Zn), were synthesized by intimately mixing MO or M_2O_3 and MoO_2 with a small stoichiometric excess of MO, where M = (Mg, Ni) in an agate mortar and pestle, followed by compression into a pressed pellet and sealing in an alumina crucible in a quartz ampoule evacuated to 10^{-2}mm Hg. The samples were first heated at 200 °C/hr to 950 °C, held at that temperature overnight, and then quenched by removal of the quartz ampoule from the furnace to the benchtop to cool. Successive regrinding, repressing, resealing, and overnight reheating cycles, with the sample placed directly into and removed from a furnace at $T = 950$°C, were performed until phase purity was achieved. Purity was checked with Rietveld refinements of powder x-ray diffraction (PXRD) patterns.

B. Nuclear and magnetic structural characterization

PXRD patterns were collected on a Bruker D8 Focus diffractometer with a LynxEye detector using Cu Kα radiation. Rietveld refinements were performed using Topas 4.2 (Bruker). Neutron powder diffraction (NPD) experiments on $Ni_2Mo_3O_8$ and $MgNiMo_3O_8$ were performed at the National Institute for Standards and Technology Center for Neutron Research (NCNR) on the BT-1 powder diffractometer using the Ge311 monochromator, 60' collimation, and a wavelength $\lambda_{neutron} = 2.0775$ Å. Nuclear structural refinements were performed using GSAS [39] and EXPGUI [40] and cross referenced with structural refinements done in the FULLPROF Suite [41]. Time-of-flight neutron powder diffraction experiments were done at the high-resolution powder diffractometer POWGEN at Oak Ridge National Laboratory using Frame 1.5 at $T = 10$ and $T = 300$ K. LeBail unit-cell refinements were used to account for the starting material (NiO, MgO, MoO_2) and side product ($NiMoO_4$) impurities, present at the <2% level.

The magnetic unit cell was manually indexed using GSAS and EXPGUI and confirmed using k-search in the FULLPROF suite. SARAh Representational Analysis software [42] and FULLPROF were used in tandem to determine the final structure. Structures were visualized using VESTA software [43].

C. Physical properties characterization

Magnetization and heat-capacity measurements were done using a Quantum Design Physical Properties Measurement System. Temperature-dependent magnetization data were collected from T = (2–300) K under applied fields of $\mu_0 H$ = 0.5 and 1 T. Susceptibility was computed as $\chi = \Delta M/\Delta H$ numerically from the two fields for each temperature. The 0.5 and 1 T fields were chosen as representative of a linear portion of the magnetization curve. Curie-Weiss analysis was performed over the temperature range $150 < T < 300$ K after linearization of the susceptibility data with a temperature-independent χ_0.

Zero-field heat capacity was collected from $T = 2$ to T = 300 K for $Ni_2Mo_3O_8$ and to $T = 150$ K for $MgNiMo_3O_8$ and $FeNiMo_3O_8$ using the semiadiabatic pulse technique with a 2% temperature rise and measurement over three time constants in time. Measurements were performed in triplicate. Field-dependent heat capacity was collected up to $\mu_0 H = 5$ T from $T = 2$ to $T = 20$ K. $Ni_2Mo_3O_8$ and $MgNiMo_3O_8$ were measured as pressed pellets, while $FeNiMo_3O_8$ was pressed with clean silver powder. Heat-capacity measurements in the $T = 150$ mK–3.5 K range were done on a Quantum Design Dilution Refrigerator (DR) using the semiadiabatic pulse technique with a 2% temperature rise and measurement over three time constants in time. Measurements were performed in triplicate. DR samples were pressed with clean silver powder to enhance thermal conductivity with the stage. In both cases, the heat capacity of silver was measured and subtracted from the raw signal.

The phononic contribution of $Ni_2Mo_3O_8$ was found by scaling the measured heat capacity of $Zn_2Mo_3O_8$ for the mass difference between nickel and zinc [44]. Similarly, the phononic contribution to the heat capacity of $MgNiMo_3O_8$ was found as the average of measurements on $Mg_2Mo_3O_8$ and $Zn_2Mo_3O_8$, scaled to account for the mass differences in the stoichiometric formulas. Literature reports on $Fe_2Mo_3O_8$ were used to scale measurements taken on $Zn_2Mo_3O_8$ to find the phonon contribution in $FeNiMo_3O_8$ [45].

D. Calculation methods

The energy splitting of the Ni^{2+} ions was calculated with a point charge model [46] using the PYCRYSTALFIELD software package [47]. Crystal electric field models were built using the ligand positions determined from the neutron diffraction experiments. The eigenstates of a single-ion Hamiltonian were calculated with crystal fields and spin-orbit coupling treated nonperturbatively. Further details are given in the Supplemental Material (SM) [48].

III. RESULTS

A. Nuclear structural determination

$Ni_2Mo_3O_8$, $MgNiMo_3O_8$, and $FeNiMo_3O_8$ are isostructural and comprised of alternating layers of hexagonal honeycomb and trimerized molybdenum oxide layers. Analyses of NPD [Figs. 1(a) and 1(b)] and PXRD patterns support that $Ni_2Mo_3O_8$, $MgNiMo_3O_8$, and $FeNiMo_3O_8$ crystallize in the noncentrosymmetric hexagonal space group 186, $P6_3mc$; see Table I.

The honeycomb lattice is a bipartite lattice comprised of two triangular sublattices. In $Ni_2Mo_3O_8$, one triangular sublattice is octahedrally coordinated Ni^{2+} and the other is tetrahedrally coordinated Ni^{2+} [49,50], making this material an integer-spin honeycomb; see Fig. 1(c). In $MgNiMo_3O_8$, 86(3)% of the 2*b* octahedral sites and 14(3)% of the 2*b* tetrahedral sites are occupied by nickel, and 14(3)% and 86(3)% of these sites, respectively, are occupied by nonmagnetic magnesium ions. The sensitivity of the fit statistics to changes in stoichiometry is shown in Fig. 1 of the SM [48]. At $T = 15$ K, the oxygen ligands on the 2*b* Wycoff position in $Ni_2Mo_3O_8$ are slightly distorted in the *c* direction from their ideal positions around the nickel sites. In the octahedron, the O-Ni-O angle is 88.2(2)° rather than the ideal 90°. In the tetrahedron, the O-Ni-O angle is 114.52(14) °, rather than the ideal 109.5°. This distortion has an anisotropic temperature dependence, shown in Fig. 2. The *c*-lattice parameter decreases almost linearly from $T = 300$ to $T = 15$ K, while the *a*-lattice parameter decreases more rapidly than *c* from $T = 300$ to $T \approx 180$ K and remains relatively constant from $T = 150$ to $T = 15$ K. The ratio of the lattice parameters *a*/*c* over temperature in the lower panel of Fig. 2 is particularly instructive: it increases from $T = 300$ to $T \approx 180$ K and decreases from $T = 130$ to $T = 15$ K. The oxygen ligand crystal field environment is similarly distorted in $MgNiMo_3O_8$ as it is in $Ni_2Mo_3O_8$. In these materials, the oxygen locations can be precisely located due to the scattering factor contrast available by NPD measurements.

$FeNiMo_3O_8$ was characterized using PXRD. The best refinements are obtained with the octahedral site selectively occupied by Fe^{2+}; see Table I and Fig. 3. The absolute differences between the fit statistics of varying occupation are, however, small, so Fe^{2+} cannot be conclusively placed only on the octahedral site. Indeed, the placement of Fe^{2+} on the octahedral site is somewhat surprising in light of prior literature reports [51] which place it on the tetrahedral site. While the ionic radius of Ni^{2+} is slightly smaller than that of Fe^{2+} (high spin) in both coordination number (CN) = 4, respectively, 0.55 and 0.63 pm, and CN = 6, 0.69 and 0.79 pm, which would tend to favor placement of Fe^{2+} on the octahedral site, crystal field stabilization energies would favor Ni^{2+} on the octahedral site. Nonetheless, the sharp antiferromagnetic transition in the susceptibility data (Fig. 4) does suggest preferential order of the Fe^{2+} and Ni^{2+} ions; site mixing tends to result in broadened transitions.

B. Physical properties

$Ni_2Mo_3O_8$ and $MgNiMo_3O_8$ both exhibit a peak in heat capacity at $T \approx 6$ K; see Figs. 4(a) and 4(b). It is at slightly higher temperature and is sharper in $Ni_2Mo_3O_8$, which is consistent with this material being less disordered and having stronger magnetic interactions than $MgNiMo_3O_8$. The application of a $\mu_0 H = 5$ T magnetic field causes the peak to shift

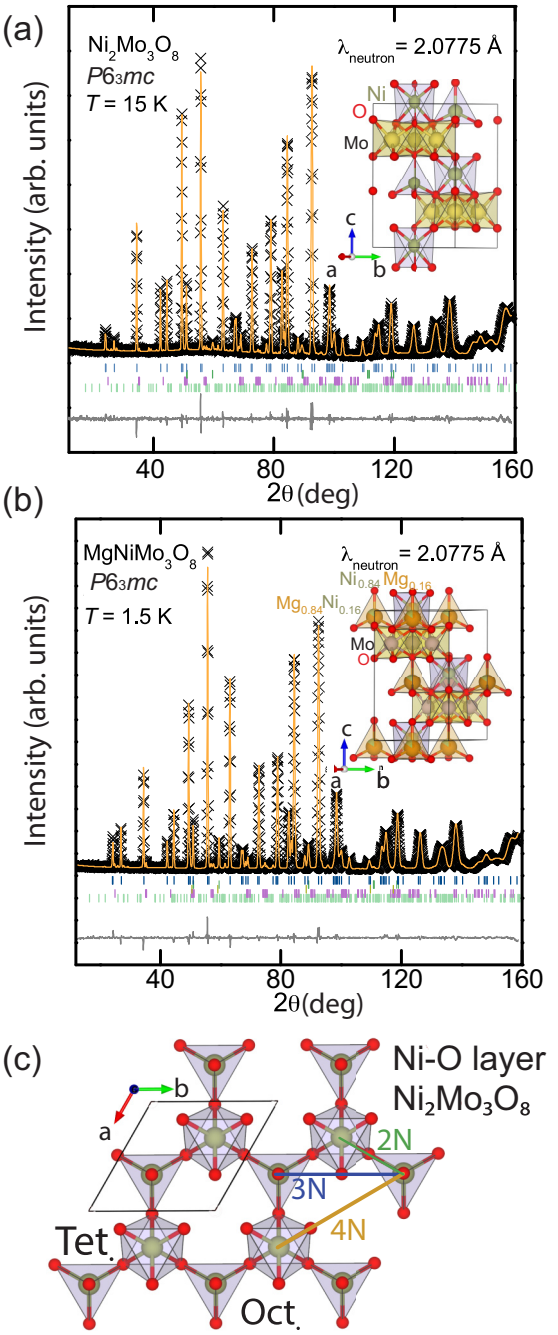

FIG. 1. Neutron powder diffraction patterns of (a) $Ni_2Mo_3O_8$ and (b) $MgNiMo_3O_8$, refined to the $P6_3mc$ space group; see Table I. Tick marks in descending vertical display order: $Ni_2Mo_3O_8$ (dark blue), NiO (dark green), MgO (brown), MoO_2 (purple), and $NiMoO_4$ (light green). MgO is not present in the refinement for $Ni_2Mo_3O_8$. (c) Top-down view of the nickel honeycomb lattice, showing alternating adjacent octahedrally and tetrahedrally coordinated atoms and nearest-neighbor [2N; 3.384(3) Å], next-nearest-neighbor [3N; 5.759(5) Å], and next-next-nearest-neighbor [4N; 6.680(5) Å] interactions. Values in parentheses indicate one standard deviation in the final digit.

TABLE I. Atomic parameters for structural refinement of $(M1)(M2)Mo_3O_8$, $M1 = (Ni, Mg, Fe)$, $M2 = Ni$; $Ni_2Mo_3O_8$ and $MgNiMo_3O_8$ from NPD (BT-1) at $T = 15$ and $T = 1.5$ K, respectively, with $\lambda_{neutron} = 2.0775$ Å, $FeNiMo_3O_8$ from PXRD at room temperature with $\lambda_{Cu,K\alpha} = 1.5406$ Å. Occupancies of $M1$ and $M2$ are given as (Mg or Fe)/Ni and Ni/(Mg or Fe), respectively. Values in parentheses indicate one standard deviation in the final figures.

		$Ni_2Mo_3O_8$	$MgNiMo_3O_8$	$FeNiMo_3O_8$
	a(Å^2)	5.74683(5)	5.75166(3)	5.76580(2)
	c(Å^2)	9.8626(2)	9.85620(9)	9.90929(3)
	T (K)	15	1.5	295
$M1$	x	1/3	1/3	1/3
2b	y	2/3	2/3	2/3
	z	0.9480(4)	0.9452(2)	0.9715(2)
	U_{iso}	0.0057(7)	0.0006(4)	0.0109(3)
	Occ.	1	0.86/0.14(3)	1.0(1)/0.0
$M2$	x	1/3	1/3	1/3
2b	y	2/3	2/3	2/3
	z	0.5116(3)	0.5120(5)	0.5348(2)
	U_{iso}	0.0056(8)	0.00106(4)	0.0109(3)
	Occ.	1	0.86/0.14(3)	1.0(1)/0
Mo	x	0.1440(2)	0.14586(9)	0.14688(3)
6c	y	–0.1440(2)	–0.14586(9)	–0.14688(3)
	z	0.2489(2)	0.25017(14)	0.2733(10)
	U_{iso}	0.0042(7)	0.0002(2)	0.0058(2)
O1	x	0	0	0
2a	y	0	0	0
	z	0.6839(5)	0.3890(3)	0.6165(4)
	U_{iso}	0.008(2)	0.0095(8)	1
O2	x	1/3	1/3	1/3
2b	y	2/3	2/3	2/3
	z	0.1461(4)	0.147(2)	0.1765(4)
	U_{iso}	0.0012(13)	0.0003(5)	1
O3	x	0.4880(3)	0.4878(2)	0.4882(2)
6c	y	–0.4880(3)	–0.4878(2)	–0.4882(2)
	z	0.3659(3)	0.36774(17)	0.3971(4)
	U_{iso}	0.0044(4)	0.0047(3)	1
O4	x	0.1688(3)	0.1723(2)	0.1665(3)
6c	y	–0.1688(3)	–0.1723(2)	–0.1665(3)
	z	0.6342(3)	0.36774(17)	0.6609(2)
	U_{iso}	0.0015(7)	0.0173(4)	1
	wRp	0.0715	0.0415	2.88
	Rp	0.0521	0.0288	2.23
	χ^2	2.526	3.913	1.41

to lower temperatures in $Ni_2Mo_3O_8$ and to higher temperatures in $MgNiMo_3O_8$, which is indicative of antiferromagnetic and ferro/ferrimagnetic orders, respectively.

Strikingly, $Ni_2Mo_3O_8$ and $MgNiMo_3O_8$ recover the same amount of entropy per magnetic ion by $T \approx 150$ K. The entropy loss looks to be two step: one degree of freedom is lost between $T = 10$ and $T = 150$ K and two more at the $T \approx 6$ K transition. The high-temperature phonon contribution, calculated from the mass-adjusted measured heat capacity of nonmagnetic analogs, describes the high-temperature behavior of the materials well. This is highlighted in the insets, which are plotted on a linear temperature scale. There is a large peak in the heat capacity of $FeNiMo_3O_8$ at $T \approx 150$ K that recovers

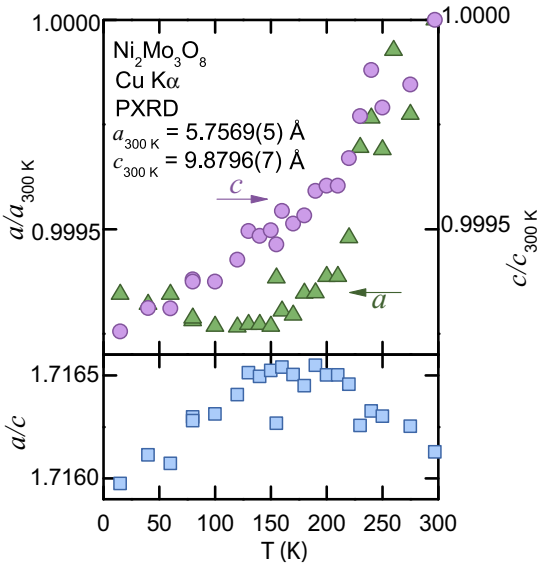

FIG. 2. Top panel: temperature dependence of the a (green triangles) and c (purple circles) lattice parameters of $Ni_2Mo_3O_8$ relative to $T = 300$ K values of 5.75695(7) Å and 9.87967(9) Å, respectively. Bottom panel: temperature dependence of the ratio of the lattice parameters (blue squares).

$\Delta S = 20.54(5)\,\mathrm{J\,mol^{-1}\,K^{-1}}$, between $T = 2$ and $T = 100$ K; see Fig. 5. The phononic background is consistent with reports on the related compound $Fe_2Mo_3O_8$ [45]. The changes in entropy of all three compounds are summarized in Table II.

All three compounds exhibit Curie-Weiss behavior at $T > 100$ K; see Fig. 6(a). $MgNiMo_3O_8$ has a small positive

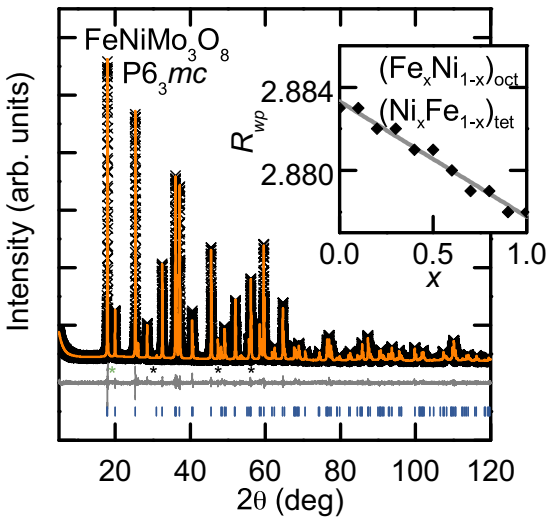

FIG. 3. Powder x-ray diffraction pattern of $FeNiMo_3O_8$ (black crosses) at room temperature with $\lambda_{Cu,K\alpha} = 1.5406$ Å, the fit of a nuclear structure model in the $P6_3mc$ space group (orange curve, blue tick marks), and the difference between them (gray curve). Black asterisks denote a silicon standard and the green asterisk a 1.6(2)% MoO_2 impurity. Inset: dependence of the R_{wp} fit statistic on Fe and Ni occupancy in $(Fe_xNi_{1-x})_{oct}$ $(Ni_xFe_{1-x})_{tet}Mo_3O_8$, where $x = 1$ represents full occupation of Fe on the octahedral site.

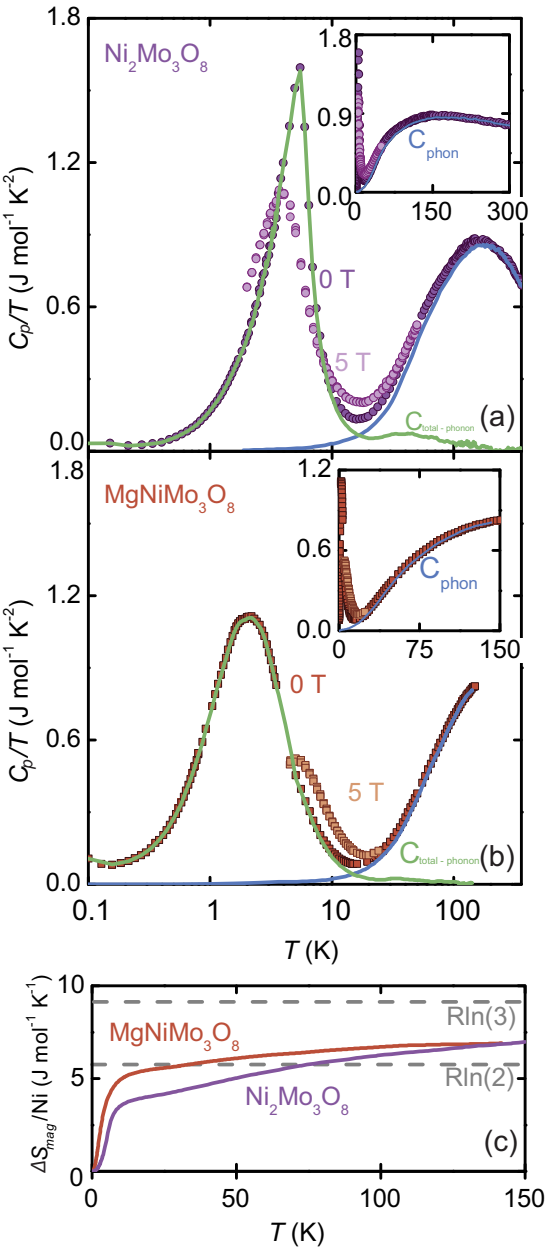

FIG. 4. (a) Heat capacity over temperature vs the logarithm of temperature of $Ni_2Mo_3O_8$ (purple circles) and (b) $MgNiMo_3O_8$ (brown squares). Magnetic heat capacity (green curve) calculated by subtracting the phononic contribution (blue curve) calculated from measured nonmagnetic analog materials. Insets: Heat capacity over temperature vs linear temperature, highlighting the high-temperature phonon contribution. (c) Change in entropy as a function of temperature, plotted per Ni ion.

Weiss temperature of $\theta_W = 6.5(1.3)$ K, consistent with weak ferromagnetic interactions, and a Curie constant of 1.280(7) and $p_{\text{eff}} = 3.20(3)\mu_B$. $Ni_2Mo_3O_8$ has a larger negative Weiss temperature of $\theta_W = -55.5(5)$ K, consistent with antiferromagnetic interactions, a total Curie constant of 5.518(1.0), and an average p_{eff} of $4.70(3)\mu_B$ per nickel atom, summarized in Table III. $FeNiMo_3O_8$ exhibits a clear antiferromagnetic phase transition at $T \approx 150$ K; see Fig. 5(b). The effective magnetic moment is 6.86(4) μ_B, which is close to the expected spin-only moment of 7.32 μ_B of combined high-spin Fe^{2+} (4.49 μ_B) and Ni^{2+} (2.83 μ_B). The Weiss temperature is $T = -101.5(3)$ K, indicating strong antiferromagnetic interactions.

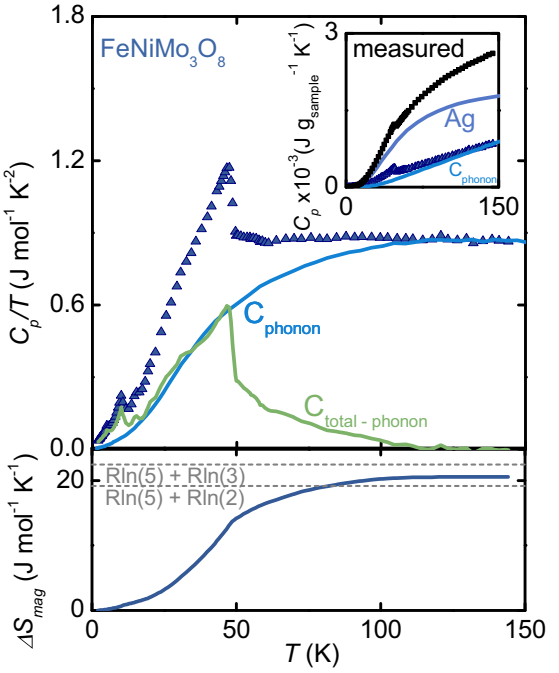

FIG. 5. Top panel: Heat capacity over temperature vs temperature of $FeNiMo_3O_8$ measured from $T = 2$ to $T = 150$ K (dark blue squares). Inset: Raw measured data (black squares) included heat capacity from clean silver powder pressed with the sample (blue curve), which was subtracted to isolate the contribution from $FeNiMo_3O_8$ (blue triangles). A peak at $T = 50$ K capturing between Rln(5) + Rln(2) and Rln(5) + Rln(3) of entropy (bottom panel, dark-blue curve) was determined to be magnetic (green curve, top panel) by subtracting the phonon contribution to the specific heat (light-blue curve, top panel and inset), from the measured nonmagnetic analog $Zn_2Mo_3O_8$ scaled to be consistent with the literature measurements on $Fe_2Mo_3O_8$ [45].

At $T = 2$ and $T = 6$ K, the field-dependent magnetization of $Ni_2Mo_3O_8$ has metamagnetic curvature which is not visible at $T = 15$ K; see Fig. 6(a) inset. Such metamagnetism suggests that a low-lying (in field) magnetic phase transition is possible. This behavior could be interpreted as differences in in-plane and out-of-plane magnetic responses, for which single-crystal samples are necessary to fully understand the nature of the transition [8]. There is no apparent hysteresis to the curve, suggesting that there is little to no ferromagnetic component of the magnetization at this temperature. The magnetic response of $MgNiMo_3O_8$ fits well to a Brillouin

TABLE II. Summary of recovered entropy per formula unit (f.u.), shown in Fig. 4(c) and the lower panel of Fig. 5.

	ΔS_{mag}(J mol-f.u.$^{-1}$K^{-1})
$Ni_2Mo_3O_8$	13.9(7)
$MgNiMo_3O_8$	6.9(3)
$FeNiMo_3O_8$	20.5(1.0)

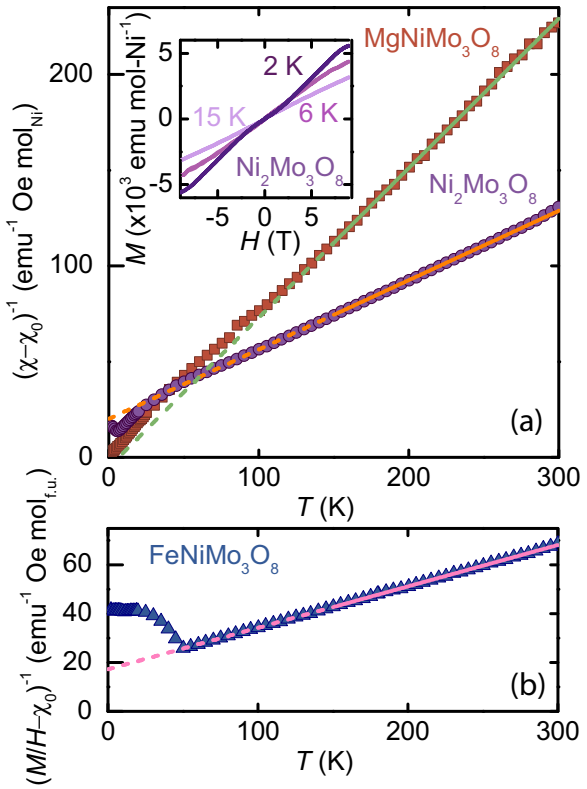

FIG. 6. Inverse susceptibility of $Ni_2Mo_3O_8$ (purple circles), $MgNiMo_3O_8$ (brown squares), and $FeNiMo_3O_8$ (blue triangles) linearized and fit to the Curie-Weiss law in the temperature range of $T = 150$ to 300 K; fit values summarized in Table III. (a) Inverse susceptibility of $MgNiMo_3O_8$ is nonlinear below $T = 150$ K, but shows no clear ordering transition. In contrast, a small upturn at $T = 6$ K in the inverse susceptibility of $Ni_2Mo_3O_8$ indicates an antiferromagnetic phase transition. The inverse susceptibility of this material is nonlinear in the $T = 6$ to 150 K temperature range. Inset: Magnetization vs applied field of $Ni_2Mo_3O_8$ at $T = 2$, 6, and 15 K. (b) A sharp uptick in the inverse susceptibility of $FeNiMo_3O_8$ indicates a clear antiferromagnetic phase transition at $T \approx 150$ K. 1Oe = $(1000/4\pi)$A/m and 1 emu/(molOe) = $4\pi\,10^{-6}$m^3/mol.

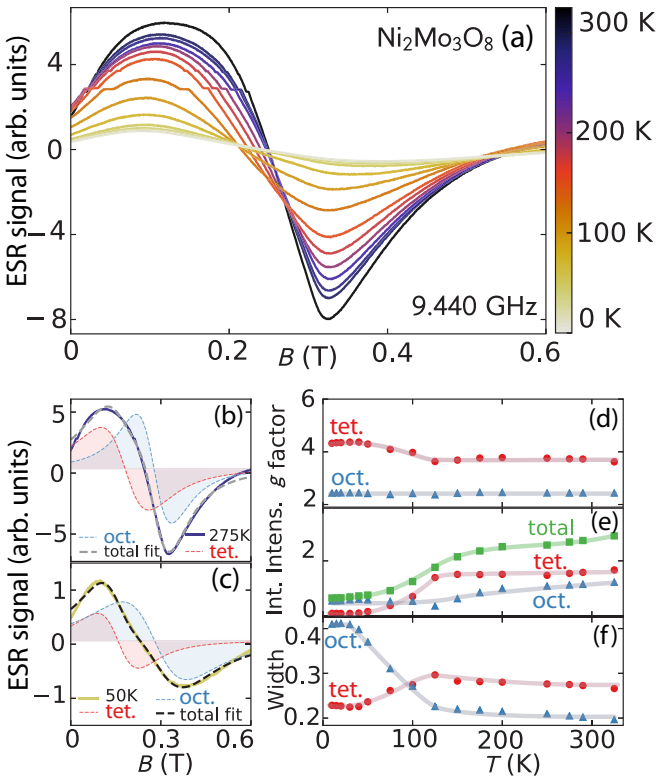

FIG. 7. (a) Temperature-dependent electron spin resonance (ESR) signal of $Ni_2Mo_3O_8$ in the $T = 10$ to $T = 325$ K range. Two Lorenzian peak profiles were used to fit the data, shown for (b) $T = 275$ K and (c) $T = 50$ K, and the (d) g factor, (e) integrated intensity, and (f) width have a temperature dependence for the tetrahedral (red circles) and octahedral (blue triangles) coordination environments. Total integrated intensity is represented with green squares. Guides to the eye are drawn for (d)–(f).

function in the $T = 2$ to $T = 300$ K temperature range and is thus likely paramagnetic at all measured temperatures (see Fig. 2 and Table I, SM [48]).

C. Electron spin resonance

The electron spin response (ESR) data in Figs. 8(a) and 8(b) from $Ni_2Mo_3O_8$ and $MgNiMo_3O_8$ have broad resonances, which is typical of $S = 1$ systems [52]. There are two magnetic sites in each unit cell: the octahedrally coordinated and tetrahedrally coordinated nickels on the two triangular honeycomb sublattices. In $Ni_2Mo_3O_8$, these sites are equally populated. In $MgNiMo_3O_8$, 14(3)% of the tetrahedral sites and 86(3)% of the octahedral sites are populated by Ni (determined from NPD), and the remaining sites are nonmagnetic. Thus, the ESR data from $Ni_2Mo_3O_8$ should show two equally weighted resonances and the data from $MgNiMo_3O_8$ should show two resonances at 14% and 86% on each of the respective sites. This is visually consistent with the data, shown in Fig. 7 for $Ni_2Mo_3O_8$, and Fig. 8 for $MgNiMo_3O_8$. The resonance for $Ni_2Mo_3O_8$ looks like one broad resonance, which can be decomposed into two similarly sized overlapping features. The resonance for $MgNiMo_3O_8$ is clearly two components. These features were fit using two Lorentzian curves, from which the g factor, integrated intensity, and width could be extracted. The temperature dependence of these parameters is plotted in Figs. 7(d)–7(f) and Figs. 8(d)–8(f).

We can leverage our knowledge of the stoichiometry and site occupancy in $MgNiMo_3O_8$ and the measured signals from $Ni_2Mo_3O_8$ and $MgNiMo_3O_8$ to separate the signals from the two sites. The higher-intensity feature in $MgNiMo_3O_8$

TABLE III. Fit values for Curie-Weiss analysis of high-temperature magnetic susceptibility of $Ni_2Mo_3O_8$, $MgNiMo_3O_8$, and $FeNiMo_3O_8$, shown graphically in Fig. 6. C and p_{eff} are per formula unit. 1Oe = $(1000/4\pi)$A/m.

	$Ni_2Mo_3O_8$	$MgNiMo_3O_8$	$FeNiMo_3O_8$
C(emu K mol^{-1} K^{-1})	5.52(1.4)	1.28(7)	5.89(9)
p_{eff}(μ_B)	6.64(6)	3.20(3)	6.86(4)
θ_W (K)	–55.5(5)	6.5(1.3)	–101(1.0)
T_N(K)	6.0(2)		50.0(2)
χ_0(emu mol^{-1} Oe^{-1})	0.0025	0.0015	0.00055

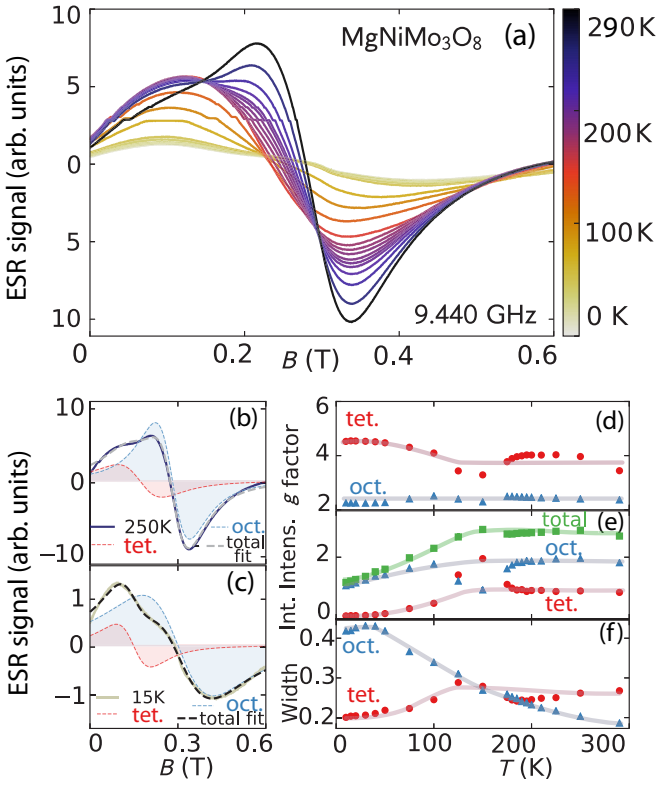

FIG. 8. (a) Temperature-dependent electron spin resonance (ESR) signal of $MgNiMo_3O_8$ in the $T = 10$ to $T = 325$ K range. Two Lorenzian peak profiles were used to fit the data, shown for (b) $T = 275$ K and (c) $T = 50$ K, and the (d) g factor, (e) integrated intensity, and (f) width have a temperature dependence for the tetrahedral (red circles) and octahedral (blue triangles) coordination environments. Total integrated intensity is represented with green squares. Guides to the eye are drawn in (d)–(f).

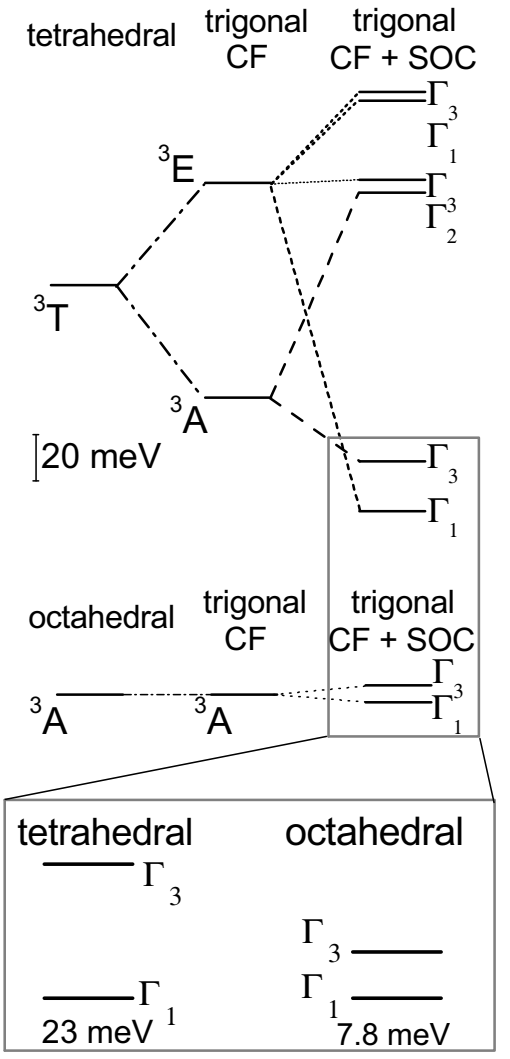

FIG. 9. Diagram of the single-ion energy levels of the undistorted tetrahedral and octahedral coordination environments (left), trigonal distortion (middle), and trigonal distortion and spin orbit coupling (SOC) (right). The two lowest-energy states of tetrahedral and octahedral crystal field environments are similar in energy splitting and have the same Γ_1 and Γ_3 representations in C_{3v}, the local symmetry of both Ni ion sites.

corresponds to the 86(3)% stoichiometric octahedral fraction, while the lower-intensity peak corresponds to the 14(3)% stoichiometric tetrahedral fraction. Subtracting the $Ni_2Mo_3O_8$ and $MgNiMo_3O_8$ signals with scaling factors for occupancy yields the single-contribution peaks (SM Fig. 3 [48]). The resonance at lower (higher) field corresponds to the tetrahedral (octahedral) component: when the scaled fraction of $Ni_2Mo_3O_8$ is subtracted from the $MgNiMo_3O_8$, the higher-field feature remains.

The g factor for the octahedral site is temperature insensitive in both $MgNiMo_3O_8$ and $Ni_2Mo_3O_8$ and remains at $\approx$2.2 from $T = 300$ to $T = 10$ K. In contrast, the g factor for the tetrahedral site remains constant at $\approx$3.7 from $T =$ 290 to $T \approx 120$ K and then increases from $T \approx 130$ K to $\approx$4.3 as temperature decreases to $T = 10$ K. Above $T =$ 150 K, the octahedral data have two isosbestic points: one at 0.28 T and the other at 0.18 T. Below $T = 150$ K, there is one isosbestic point at 0.23 T. The integrated intensity for both $Ni_2Mo_3O_8$ and $MgNiMo_3O_8$ decreases from $T \approx 150$ to $T = 10$ K.

D. Single-ion crystal field analysis

Using the low-temperature crystal structure, a point charge model can be used to construct the expected splitting of multielectron states for Ni^{2+} on the octahedral and tetrahedral sites; see Fig. 9. As expected, the trigonal distortion removes the orbital degeneracy for the tetrahedral case, but leaves the (orbitally nondegenerate) ground state of the octahedral site intact. The confluence of the trigonal crystal field with spin-orbit coupling lifts the degeneracy of the ground-state triplet, resulting in single-ion anisotropies of $\Delta = 22$ and $\Delta = 7.8$ meV for tetrahedral and octahedral, respectively. Crucially, the low-lying states on the two distinct sites are symmetry compatible and thus can have significant exchange/superexchange interactions, in agreement with the large and negative Weiss temperature observed for $Ni_2Mo_3O_8$. Further, the single-ion anisotropy of the tetrahedral site is consistent with the temperature-dependent changes observed in ESR: the g factor is expected to start to change from its high-temperature to low-temperature value around $0.42^*\Delta =$

TABLE IV. Irreducible representations (IR) and basis vectors (BV) for the two magnetic nickel atoms in $Ni_2Mo_3O_8$ and associated real components in the *a, b,* and *c* directions for $\vec{k} = (1/2\,0\,0)$ in space group $P6_3mc$.

IR	BV	Atom	$m_{\parallel a}$	$m_{\parallel b}$	$m_{\parallel c}$
Γ_1	ψ_1	Ni1	0	–1	0
		Ni2	0	–1	0
Γ_2	ψ_2	Ni1	2	1	0
		Ni2	2	1	0
	ψ_3	Ni1	0	0	2
		Ni2	0	0	–2
Γ_3	ψ_4	Ni1	0	–1	0
		Ni2	0	1	0
Γ_4	ψ_5	Ni1	2	1	0
		Ni2	–2	–1	0
	ψ_6	Ni1	0	0	2
		Ni2	0	0	2

107 K, versus the observed $T = 110$ K. In contrast, the octahedral site would not have a local change in anisotropy until ≈30 K, a temperature at which interactions between sites are already dominant. While the single-ion prediction that the lowest-energy states are singlets would seem to imply that nonmagnetic behavior is expected at low temperatures, a combination of modest superexchange interactions between the Γ_3 states (of the order of 7 meV) and/or second-order SOC could be sufficient to cause Γ_3 to be the lowest-energy state. This energy is of the same order as that implied by the Weiss temperature of –55 K (∼6 meV). The Weiss temperature likely underestimates the strength of the antiferromagnetic nearest-neighbor coupling as it encompasses all interactions and our results on $MgNiMo_3O_8$ demonstrate net ferromagnetic next-nearest-neighbor interactions.

E. Magnetic structure determination

Magnetic Bragg peaks were identified in NPD patterns of $Ni_2Mo_3O_8$ at $T = 1.6$ K that were not present at $T = 15$ K, which is consistent with the magnetic phase transition observed in susceptibility data. These peaks were isolated by subtraction of nuclear peaks measured at the two temperatures and can be seen in Fig. 4 in the SM [48]. The largest propagation vector, $\vec{k}$, the smallest vector in real space that indexes all of the magnetic peaks is $\vec{k} = (1/2\,0\,0)$. This indicates that a doubling of the unit cell in the *a* direction is necessary to describe the magnetic order. The resulting magnetic unit cell is orthorhombic. Representational analysis of this $\vec{k}$ vector in space group $P6_3mc$ leads to four irreducible representations: Γ_1, Γ_2, Γ_3, and Γ_4 on six basis vectors ψ_1-ψ_6, which are summarized in Table IV. Consistent with Landau theory, only a single irreducible representation is necessary to describe the structure resulting from a second-order phase transition.

The intensity of neutrons scattering off of long-range magnetic moments corresponds to the magnetic moment perpendicular to the neutron-scattering vector. The tallest magnetic peak at $2\theta = 24.10°$ corresponds to the (004) reflection. The intensities of this and related reflections indicates significant magnetic moment in the *c* direction. The Γ_1 and Γ_3 irreducible representations cannot have magnetic moment in the $m_{\parallel c}$ direction and thus may be discarded. Both Γ_2 and Γ_4 allow for intensity at all indexed peaks. Between the two, refinements of Γ_2, with statistical χ^2 of 4.479, show a better fit to the data than the best fit of Γ_4, which gives a χ^2 of 5.502. A comparison of the statistical refinements can be seen in Table II in the SM [48].

The magnetic orders of Ising-type spins on the honeycomb lattice can be classified by the number of ferromagnetic (FM) and antiferromagnetic (AFM) interactions between adjacent spins on a lattice. These classes of magnetic order are as follows: FM, stripy AFM, zigzag AFM, and Néel AFM, as shown in Fig. 10. The FM structure is characterized by all FM interactions on adjacent spins: each spin has three FM interactions. Néel AFM is characterized by all AFM interactions: each spin has three AFM interactions. In the zigzag AFM case, each spin has two FM and one AFM interaction. In the stripy AFM case, each spin has two AFM interactions and one FM interaction.

Spin is a vector, and a more complex order can have admixtures of these different simple orders when the strict Ising

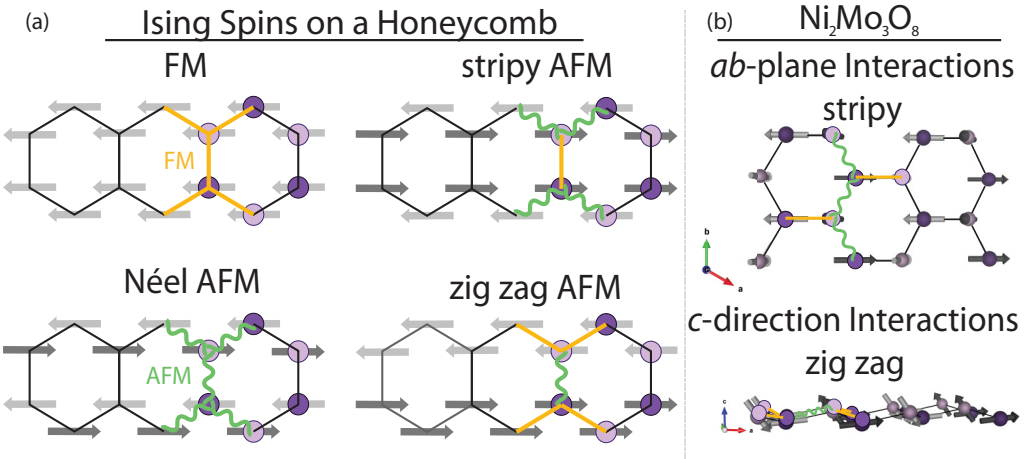

FIG. 10. (a) Magnetic order on the honeycomb lattice with Ising-type spins. (b) Visualization of the solved magnetic structure of $Ni_2Mo_3O_8$ highlighting the stripy *ab*-plane (top) and zigzag *c*-direction (bottom) components of the magnetic moment.

TABLE V. Values and ratios of tetrahedral to octahedral magnetic moments from ESR measured at $T = 10\,\mathrm{K}$ and refinements in $\mathbf{\Gamma}_2$ to the magnetic Bragg peaks from NPD with the tetrahedral spins primarily in the *ab* plane or the *c* direction.

	$\mu_{B,\mathrm{Tet.}}$	$\mu_{B,\mathrm{Oct.}}$	$\frac{\mu_{B,\mathrm{Tet.}}}{\mu_{B,\mathrm{Oct.}}}$
ESR $T = 10\,\mathrm{K}$	4.32	2.43	1.78
ab plane	1.727	1.431	1.21
c direction	1.997	0.891	2.24

constraint is relaxed. With no constraints on magnitude and direction of magnetic moment, the refined magnetic structure of $Ni_2Mo_3O_8$ is stripy AFM with respect to the *ab*-plane interactions and zigzag AFM with respect to ordering in the *c* direction, according to the above screen.

All combinations of larger moment on the tetrahedral site or the octahedral site, initiated with magnitude in the *c* direction or the *ab* plane, and every combination of positive and negative starting values for the coefficients of the basis vectors were refined using the nuclear-subtracted magnetic Bragg peaks with no constraints on magnitude and direction. All refinements resulted in equivalent magnetic structures. While there is no statistical difference between the χ^2 metric of the quality of the refinements that have more magnitude on the octahedral or tetrahedral nickel site (the sites are indistinguishable if only the Ni atom positions are considered), it is clear from ESR data that there is a larger magnetic moment on the tetrahedral nickel.

There are two statistically identical magnetic structures with larger magnetic moment on the tetrahedral nickel. There is strong directionality to the magnetic moment of the two sites of both. In one, an ordered moment of 1.727 μ_B on the tetrahedral site lies mainly in the *ab* plane and a moment of 1.431 μ_B on the octahedral site points primarily in the *c* direction. In the other, an ordered moment of 1.997 μ_B on the tetrahedral site has significant moment in the *c* direction and a moment of 0.891 μ_B on the octahedral site is mainly in the *ab* plane. The ratio of the tetrahedral to octahedral *g* factors (which are proportional to the magnetic moment) is 1.21 for a structure where the tetrahedral moment is primarily in the *ab* plane and 2.24 for the moment in the *c* direction. These numbers bracket the ratio of 1.8 observed in the ESR measurements at $T = 10\,\mathrm{K}$; see Table V. The refinement to the structure where the tetrahedral spins lie mainly in the *ab* plane better describes the data, based on visual inspection. Refinements and visualization of both structures may be seen in Fig. 4 in the SM [48]. This solution is more intuitively correct, too; one would expect the magnetic moment to be roughly the same for the two sites, as nickel is 2+ on both.

IV. DISCUSSION

The ratio of the tetrahedral site *g* factor to the octahedral site *g* factor determined by ESR at $T = 290\,\mathrm{K}$ is 1.46, which is very close to 1.52, the ratio of the effective magnetic moments per Ni of $Ni_2Mo_3O_8$ to $MgNiMo_3O_8$ found by Curie-Weiss analysis of temperature-dependent magnetization. This further validates the agreement of the magnetic measurements and the conclusion that $MgNiMo_3O_8$ is an analog for the magnetic behavior for isolated nickels interacting on the octahedrally coordinated sublattice of the honeycomb. This ratio is also close to the ratio of the ordered magnetic moments on the tetrahedral and octahedral sites determined by NPD.

The data support the interpretation that there is anisotropy to the magnetism on the tetrahedral site in $Ni_2Mo_3O_8$. (1) The ordered structure shows a strong directional dependence of the magnetic moment on the two sites where the tetrahedral site has a strong *ab*-plane component; (2) the observed metamagnetism in the field-dependent magnetization [inset, Fig. 6(a)] is a signature of anisotropy in powder samples, and has been observed in other honeycombs such as α-$RuCl_3$ [8]; and (3) the entropy recovered in heat-capacity measurements is consistent with Ni on the tetrahedral site recovering Rln(2) in $Ni_2Mo_3O_8$.

The expected recovered entropy for a triangular lattice of $S = 1$ ions with three spin degrees of freedom is Rln(3) and for a honeycomb lattice (comprised of two triangular sublattices) is 2Rln(3). As summarized in Table II, $Ni_2Mo_3O_8$ recovers ≈Rln(2) + Rln(3) and $MgNiMo_3O_8$ recovers $6.9(3)\,\mathrm{J mol^{-1}\,K^{-1}} = 0.764\mathrm{Rln}(3)$ of entropy. The site disorder determined by NPD places 86% of Ni on the octahedral site in $MgNiMo_3O_8$. The theoretical change in entropy if the octahedral site were to recover Rln(2) and the tetrahedral site were to recover Rln(3) is $6.1\,\mathrm{J\,mol^{-1}\,K^{-1}}$. As this is smaller than the recovered value, it is clear that the octahedral site must be recovering Rln(3). The value of 0.76Rln(3) suggests, but does not conclusively prove, that the tetrahedral site does not recover significant entropy in $MgNiMo_3O_8$. That the entropy in $Ni_2Mo_3O_8$ recovers Rln(3) + Rln(2) strongly suggests that the tetrahedral site recovers Rln(2) of entropy, and thus has one fewer degree of freedom than the octahedral site. This implies spin anisotropy, perhaps easy plane, which is consistent with the magnetic structure.

There are three known possible magnetic Hamiltonians which could stabilize stripy or zigzag AFM order in $Ni_2Mo_3O_8$: (1) bond-dependent Heisenberg-Kitaev interactions [24,52], (2) isotropic interactions where nearest-neighbor (2N), next-nearest-neighbor (3N), and next-next-nearest-neighbor (4N) in-plane interactions are all of similar strength [12,13], and (3) bond-dependent anisotropic interactions through ligand distortion [35,53].

(1) The Kitaev model requires that exchange anisotropy must be orthogonal to the Ni-Ni bond and that there are 90^o interfering ligand superexchange pathways for Ising-like terms to emerge [54]. In $Ni_2Mo_3O_8$, the Ni-O-Ni bond lies along a mirror plane which precludes the necessary orthogonality. In addition, the alternating octahedral and tetrahedral coordination environments geometrically obstruct the ligand superexchange pathway.

(2) Isotropic interactions can stabilize zigzag order when the 2N, 3N, and 4N in-plane interactions are all of similar strength. In $Ni_2Mo_3O_8$, 2N interactions are octahedral-tetrahedral (3.39 Å; oxygen mediated), 3N interactions are self-sublattice octahedral-octahedral and etrahedral-tetrahedral (5.96 Å; oxygen and molybdenum mediated), and 4N are octahedral-tetrahedral [6.680(5) Å]. $MgNiMo_3O_8$ can be viewed as a magnetically dilute analog of $Ni_2Mo_3O_8$ where the interacting magnetic atoms are predominantly structurally equivalent to the 3N interaction sublattice in $Ni_2Mo_3O_8$. While not a perfect analog, the type and relative scale of

the magnetic interactions in $MgNiMo_3O_8$ is suggestive of the characteristics of the $Ni_2Mo_3O_8$ 3N interactions in the absence of the 2N interactions. The result of this magnetic dilution is a dramatic loss of interaction strength: the Weiss temperature of $MgNiMo_3O_8$ is small and positive (6 K), indicating that the interactions are small and ferromagnetic. For comparison, the Weiss temperature of $Ni_2Mo_3O_8$ is -55 K. Thus it is likely that nearest-neighbor interactions are making up the bulk of the antiferromagnetic interactions in $Ni_2Mo_3O_8$ and isotropic interactions are likely not stabilizing the zigzag order.

(3) There are slight distortions of the octahedral and tetrahedral coordination environments from the ideal single-ion crystal field to the symmetry-adapted, spin-orbit-coupled regime. Both Ni^{2+} ions are on sites with $3m(C_{3v})$ symmetry, which is significantly lower point symmetry than either the O_h or T_d point groups in the single-ion regime. As described in Fig. 9, the lowest-energy state in an undistorted octahedral complex is ^{3}A, which decomposes into a singlet Γ_1 and doublet Γ_3 under small trigonal distortions and application of spin-orbit coupling in $3m$ symmetry. The next lowest-energy state is 490 meV higher. In the tetrahedral coordination, the ground state is a spin and orbital triplet, ^{3}T, which decomposes into a singlet Γ_1 and doublet Γ_3 under small trigonal distortions and application of spin-orbit coupling in $3m$ symmetry. It is possible that the bond-dependent interactions that occur as a result of Γ_1-Γ_1 and Γ_3-Γ_3 mixing in adjacent octahedral and tetrahedral coordination environments stabilize the complex order in $Ni_2Mo_3O_8$. We note that this does not require a large magnetoelastic effect, as the bond dependence arises due to differential orbital occupations; concomitance with a significant structural distortion depends on whether this change in orbital occupation couples strongly to the lattice. An example of the weak-coupling case can be found in $NaVO_2$ [55].

Bond-dependent interactions are consistent with the data collected. In particular, the rich temperature-dependent behavior in the ESR data suggest the presence of single-ion anisotropy that changes with temperature: the g factor increases between $T = 130$ and $T = 10$ K, and below $T \approx 150$ K the amplitude of the signal decreases. This is attributable to a change in the timescale of paramagnetic fluctuations to frequencies below those that ESR samples as the magnetic order approach long-range order. Additionally, the ratio of the a- and c-lattice parameters shows anisotropic changes concomitant with the temperature dependence of the ESR data. Further work is required to determine whether the noncolinear arrangement of spins between the octahedral and tetrahedral sites is due to DM interactions, single-ion anisotropies, or both.

V. CONCLUSION

$Ni_2Mo_3O_8$ is a realized example of an integer spin non-Néel AFM ordered honeycomb in a noncentrosymmetric space group ($P6_3mc$). Theoretical studies have predicted the existence of topological magnons in honeycomb compounds with stripy and zigzag AFM order, and $Ni_2Mo_3O_8$, with an ordered magnetic state characterized as an admixture of stripy and zigzag order, may provide an opportunity to investigate this and other topological phenomena experimentally without the presence of inversion symmetry. The zigzag AFM order on $Ni_2Mo_3O_8$ may be stabilized by bond-dependent anisotropic exchange due to ligand distortion. The structure of alternating octahedral and tetrahedral Ni^{2+} on the honeycomb offers fundamentally different chemistry from other nickel honeycomb compounds in existence. We have also shown that the magnetic exchanges in this material are tunable by selective chemical substitution on the honeycomb, from weakly ferromagnetic ($MgNiMo_3O_8$) to strongly antiferromagnetic ($FeNiMo_3O_8$). Further studies on these materials will advance the search for realized nontrivial quantum states of matter.

ACKNOWLEDGMENTS

This work was supported by the U.S. Department of Energy, Office of Basic Energy Sciences, Division of Materials Sciences and Engineering under Award No. DE-FG-02-08ER46544 to the Institute for Quantum Matter at Johns Hopkins University. Additional neutron-diffraction experiments were done on the POWGEN instrument at Oak Ridge National Laboratory by Ashfia Huq. T.M.M. acknowledges fruitful discussions with Andriy Nevidomskyy. J.R.M. acknowledges Zachary Kelly and Christopher Pasco for useful consultations. The authors acknowledge Jiajia Wen for measuring silver on the dilution refrigerator for data analysis purposes. T.M.M. acknowledges additional financial support from the Johns Hopkins University Catalyst Award. The dilution refrigerator was funded through the National Science Foundation Major Research Instrumentation Program, Grant No. DMR-0821005. Diagnostic measurements were done using instrumentation at the Platform for the Accelerated Realization, Analysis, and Discovery of Interface Materials (PARADIM), a National Science Foundation Materials Innovation Platform funded under Cooperative Agreement No. DMR-1539918. Certain commercial equipment, instruments, or materials are identified in this document. Such identification does not imply recommendation or endorsement by the National Institute of Standards and Technology nor does it imply that the products identified are necessarily the best available for the purpose.

[1] M. Z. Hasan and C. L. Kane, Rev. Mod. Phys. **82**, 3045 (2010).
[2] Y. Ando and L. Fu, Ann. Rev. Condens. Matter Phys. **6**, 361 (2015).
[3] Y. Zhou, K. Kanoda, and T-K. Ng, Rev. Mod. Phys. **89**, 025003 (2017).
[4] L. Savary and L. Balents, Rep. Prog. Phys. **80**, 016502 (2016).
[5] B. K. Clark, D. A. Abanin, and S. L. Sondhi, Phys. Rev. Lett. **107**, 087204 (2011).
[6] A. Kitaev, Ann. Phys. **321**, 2 (2006).
[7] K. W. Plumb, J. P. Clancy, L. J. Sandilands, V. V. Shankar, Y. F. Hu, K. S. Burch, Hae-Young Kee, and Young-June Kim, Phys. Rev. B **90**, 041112(R) (2014).

[8] J. A. Sears, M. Songvilay, K. W. Plumb, J. P. Clancy, Y. Qiu, Y. Zhao, D. Parshall, and Young-June Kim, Phys. Rev. B **91**, 144420 (2015).

[9] H.-S. Kim, V. Vijay Shankar, A. Catuneanu, and H.-Y. Kee, Phys. Rev. B **91**, 241110(R) (2015).

[10] A. Banerjee, C. A. Bridges, J.-Q. Yan, A. A. Aczel, L. Li, M. B. Stone, G. E. Granroth, M. D. Lumsden, Y. Yiu, J. Knolle, S. Bhattacharjee, D. L. Kovrizhin, R. Moessner, D. A. Tennant, D. G. Mandrus, and S. E. Nagler, Nat. Mater. **15**, 733 (2016).

[11] A. Banerjee, P. Lampen-Kelley, J. Knolle, C. Balz, A. A. Aczel, B. Winn, Y. Liu, D. Pajerowski, J. Yan, C. A. Bridges, A. T. Savici, B. C. Chakoumakos, M. D. Lumsden, D. A. Tennant, R. Moessner, D. G. Mandrus, and S. E. Nagler, Npj Quantum Mater. **3**, 8 (2018).

[12] P. H. Y. Li, R. F. Bishop, D. J. J. Farnell, and C. E. Campbell, Phys. Rev. B **86**, 144404 (2012).

[13] A. F. Albuquerque, D. Schwandt, B. Hetényi, S. Capponi, M. Mambrini, and A. M. Läuchli, Phys. Rev. B **84**, 024406 (2011).

[14] Y.-Z. You, I. Kimchi, and A. Vishwanath, Phys. Rev. B **86**, 085145 (2012).

[15] J. Reuther, R. Thomale, and S. Rachel, Phys. Rev. B **90**, 100405 (R)(2014).

[16] A. Biffin, R. D. Johnson, I. Kimchi, R. Morris, A. Bombardi, J. G. Analytis, A. Vishwanath, and R. Coldea, Phys. Rev. Lett. **113**, 197201 (2014).

[17] T. Takayama, A. Kato, R. Dinnebier, J. Nuss, H. Kono, L. S. I. Veiga, G. Fabbris, D. Haskel, and H. Takagi, Phys. Rev. Lett. **114**, 077202 (2015).

[18] S. C. Williams, R. D. Johnson, F. Freund, S. Choi, A. Jesche, I. Kimchi, S. Manni, A. Bombardi, P. Manuel, P. Gegenwart, and R. Coldea. Phys. Rev. B **93**, 195158 (2016).

[19] H-C. Jiang, Z-C. Gu, X-L. Qi, and S. Trebst, Phys. Rev. B **83**, 245104 (2011).

[20] Y. Singh, S. Manni, J. Reuther, T. Berlijn, R. Thomale, W. Ku, S. Trebst, and P. Gegenwart, Phys. Rev. Lett. **108**, 127203 (2012).

[21] F. Ye, S. Chi, H. Cao, B. C. Chakoumakos, J. A. Fernandez-Baca, R. Custelcean, T. F. Qi, O. B. Korneta, and G. Cao, Phys. Rev. B **85**, 180403(R) (2012).

[22] J. Chaloupka, G. Jackeli, and G. Khaliullin, Phys. Rev. Lett. **110**, 097204 (2013).

[23] V. M Katukuri, S. Nishimoto, V. Yushankhai, A. Stoyanova, H. Kandpal, S. Choi, R. Coldea, I. Rousochatzakis, L. Hozoi, and J. van den Brink, New J. Phys. **16**, 013056 (2014).

[24] K. A. Modic, T. E. Smidt, I. Kimchi, N. P. Breznay, A. Biffin, S. Choi, R. D. Johnson, R. Coldea, P. Watkins-Curry, G. T. McCandless, J. Y. Chan, F. Gandara, Z. Islam, A. Vishwanath, A. Shekhter, R. D. McDonald, and J. G. Analytis, Nat. Commun. **5**, 4203 (2014).

[25] J. Chaloupka and G. Khaliullin, Phys. Rev. B **94**, 064435 (2016).

[26] F. Mezzacapo and M. Boninsegni, Phys. Rev. B **85**, 060402(R) (2012).

[27] J. G. Rau, Eric Kin-Ho Lee, and H.-Y. Kee, Phys. Rev. Lett. **112**, 077204 (2014).

[28] Z. Nussinov and J. van den Brink, Rev. Mod. Phys. **87**, 1 (2015).

[29] E. A. Zvereva, M. I. Stratan, A. V. Ushakov, V. B. Nalbandyan, I. L. Shukaev, A. V. Silhanek, M. Abdel-Hafiez, S. V. Streltsovbh, and A. N. Vasilievahi, Dalton Trans. **45**, 7373 (2016).

[30] H. Liu and G. Khaliullin, Phys. Rev. B **97**, 014407 (2018).

[31] S. A. Owerre, J. Phys. Condens. Matter **28**, 386001 (2016).

[32] H. Lee, S. B. Chung, K. Park, and J.-G. Park, arXiv:1712.09801 (2017).

[33] S. A. Owerre, Phys. Rev. B **95**, 014422 (2017).

[34] S. P. McAlister and P. Strobel, J. Magn. Magn. Mater. **20**, 3 (1983).

[35] E. A. Zvereva, M. I. Stratan, Y. A. Ovchenkov, V. B. Nalbandyan, J.-Y. Lin, E. L. Vavilova, M. F. Iakovleva, M. Abdel-Hafiez, A. V. Silhanek, X.-J. Chen, A. Stroppa, S. Picozzi, H. O. Jeschke, R. Valenti, and A. N. Vasiliev, Phys. Rev. B **92**, 144401 (2015).

[36] E. M. Seibel, J. H. Roudebush, H. Wu, Q. Huang, M. N. Ali, H. Ji, and R. J. Cava, Inorg. Chem. **52**, 13605 (2013).

[37] R. Berthelot, W. Schmidt, S. Muir, J. Eilertsen, L. Etienne, A. W. Sleight, and M. A. Subramanian, Inorg. Chem. **51**, 5377 (2012).

[38] T. Kurumaji, S. Ishiwata, and Y. Tokura, Phys. Rev. X **5**, 031034 (2015).

[39] A. C. Larson and R. B. Von Dreele, Los Alamos National Laboratory Report, Los Alamos National Laboratory, Los Alamos, New Mexico, USA, LAUR 86–748 (2000).

[40] B. H. Toby, J. Appl. Cryst. **34**, 210 (2001).

[41] J. Rodrigues-Carvajal, Phys. B **192**, 55 (1993).

[42] A. S. Wills, Phys. B **276**, 680 (2000).

[43] K. Momma and F. Izumi, J. Appl. Cryst. **44**, 1272 (2011).

[44] A. Tari, *The Specific Heat of Matter at Low Temperatures* (Imperial College Press, London, 2003).

[45] T. Kurumaji, Y. Takahashi, J. Fujioka, R. Masuda, H. Shishikura, S. Ishiwata, and Y. Tokura, Phys. Rev. B **95**, 020405 (R)(2017).

[46] M. Hutchings, Solid State Phys. **16**, 227 (1964).

[47] A. Scheie, PyCrystalField, GitHub repository, https://github.com/asche1/PyCrystalField (2018).

[48] See Supplemental Material at http://link.aps.org/supplemental/10.1103/PhysRevMaterials.3.014410 for additional structural data and physical properties characterization.

[49] W. H. McCarroll, L. Katz, and R. Ward, J. Am. Chem. Soc. **79**, 5410 (1957).

[50] P. Strobel, Y. Le Page, J. Cryst. Growth **61**, 329 (1983).

[51] F. Varret, H. Czeskleba, F. Hartmann-Boutron, and P. Imbert, J. Phys. France, **33**, 549 (1972).

[52] A. Abragam and B. Bleaney, *Electron Paramagnetic Resonance of Transition Ions*, 1st ed. (Clarendon, Oxford, 1970).

[53] H. B. Cao, A. Banerjee, J.-Q. Yan, C. A. Bridges, M. D. Lumsden, D. G. Mandrus, D. A. Tennant, B. C. Chakoumakos, and S. E. Nagler, Phys. Rev. B **93**, 134423 (2016).

[54] G. Jackeli and G. Khaliullin, Phys. Rev. Lett. **102**, 017205 (2009).

[55] T. M. McQueen, P. W. Stephens, Q.-Z. Huang, T. Klimczuk, F. Ronning, and R. J. Cava, Phys. Rev. Lett. **101**, 166402 (2008).